

On the Impossibility of High-Density Electrostatic Energy Storage at Low Voltage and the Necessity of a Chemical Mechanism in Nanostructured Metal Oxide/Carbon Composite Devices

Albert J. Feher

Independent Researcher, DeLand, Florida, USA

March 31, 2026

Abstract

This paper presents a quantitative argument that energy storage devices based on nanostructured metal oxide/carbon composites operating at cell voltages of 1–4 V cannot store energy at densities exceeding approximately 100 Wh/kg through electrostatic field energy alone, regardless of electrode nanostructure, dielectric permittivity, or interfacial area. The fundamental limitation is the energy density of electric fields: $\frac{1}{2}E^2\epsilon_0\epsilon$ yields values many orders of magnitude below the reported performance of recently announced devices. Any device in this class achieving energy densities of 200–400 Wh/kg must therefore store the majority of its energy through a chemical mechanism. The most physically plausible chemical mechanism in a system containing amorphous metal oxide, carbon, and bound water is field-driven proton intercalation into the amorphous oxide lattice, where the electrostatic field generated by the capacitor architecture provides the driving force for proton insertion and extraction. This paper derives the quantitative constraints, evaluates the proton intercalation hypothesis against published third-party performance data, and identifies the observable signatures that would confirm or refute the proposed mechanism.

1. Introduction

Recent announcements of solid-state energy storage devices employing metal oxide/carbon composite electrodes fabricated by aqueous screen printing have reported energy densities in the range of 300–400 Wh/kg, rivaling or exceeding lithium-ion batteries. These devices have been variously described as solid-state batteries, supercapacitors, and electrostatic capacitors. Third-party testing has confirmed fast-charging capability, high-temperature stability, battery-like charge retention, and mechanical robustness, but the internal chemistry and energy storage mechanism have not been publicly disclosed.

The absence of disclosed chemistry has generated significant debate about whether these devices operate as batteries, capacitors, or some hybrid mechanism. This paper approaches the question from first principles: given the known constraints of electrostatic energy storage at low voltage, what mechanisms are physically capable of producing the observed performance?

The analysis leads to a definitive conclusion on what the mechanism *cannot* be, and a constrained hypothesis about what it *could* be, with quantitative predictions that are experimentally testable.

2. The Electrostatic Energy Density Limit

2.1 Bulk Field Energy

The energy density of an electric field in a dielectric medium is:

$$u = \frac{1}{2}\epsilon_0\epsilon E^2$$

where ϵ_0 is the vacuum permittivity (8.85×10^{-12} F/m), ϵ is the relative permittivity of the dielectric, and E is the electric field strength. For a parallel-plate geometry with voltage V across a gap of thickness d , $E = V/d$.

Consider the most favorable case: a high-permittivity dielectric ($\epsilon = 1000$, comparable to BaTiO_3) at the maximum voltage of a typical cell ($V = 4$ V) across a thin separator ($d = 10 \mu\text{m} = 10^{-5}$ m). The field strength is $E = 4 \times 10^5$ V/m.

The energy density is $u = \frac{1}{2} \times 8.85 \times 10^{-12} \times 1000 \times (4 \times 10^5)^2 = 0.71$ J/m³.

For a separator of area 200 cm² and thickness 10 μm , the total volume is 2×10^{-7} m³ and the stored energy is 1.4×10^{-7} J. This is approximately 140 nanojoules. To put this in perspective: a representative device in this class has a nominal energy of 94 Wh (338,400 J). The ratio of required energy to the available electrostatic field energy is $338,400 / 1.4 \times 10^{-7} = 2.4 \times 10^{12}$ — a deficit of approximately twelve orders of magnitude.

It should be noted that this calculation is conservative — that is, it overstates the energy available from electrostatic storage. The calculation considers only the separator dielectric and assigns all of the stored energy to the electric field within it. In a real device, the total mass includes not only the separator but also the electrodes, current collectors, binder, and packaging, none of which contribute to the electrostatic field energy. Including these inactive components in the energy density calculation would reduce the device-level electrostatic energy density still further, widening the deficit beyond twelve orders of magnitude. The 140 nanojoules therefore represents an upper bound on the electrostatic contribution, not a realistic estimate.

This calculation is not sensitive to the assumed parameters. Increasing ϵ to 10,000 (beyond any known solid dielectric at room temperature) gains one order of magnitude. Reducing d to 1 μm gains two orders of magnitude (through increased E). Together these extreme assumptions recover only three orders of magnitude of the twelve-order deficit. **No physically realizable combination**

of permittivity and geometry can store 94 Wh of electrostatic field energy at cell voltages of 1–4 V.

2.2 Nanostructured Interface Energy

One might argue that nanostructured electrodes with enormous internal surface area could store energy in nanoscale interfacial fields rather than in the bulk separator field. Consider a generous case: a nanocomposite with 1000 m²/g of conductor/dielectric interface (a high but achievable value for nanostructured carbons, though below the theoretical maximum of ~2630 m²/g for single-layer graphene), with a 1 nm dielectric layer of $\epsilon = 80$ (the permittivity of bulk water, noting that nanoconfined water may exhibit substantially lower permittivity, potentially as low as 2–10 in sub-nanometer confinement, which would reduce this estimate further) at 1 V across each interface.

The interfacial capacitance per unit area is $C = \epsilon_0 \epsilon / d = 8.85 \times 10^{-12} \times 80 / 10^{-9} = 0.71 \text{ F/m}^2$. Over 1000 m², the total capacitance is 710 F/g. The energy per gram is $E = \frac{1}{2} CV^2 = \frac{1}{2} \times 710 \times 1^2 = 355 \text{ J/g} = 98.6 \text{ Wh/kg}$.

This is an upper bound under extremely optimistic assumptions: a high specific surface area, the permittivity of bulk water (which nanoconfined water is unlikely to exhibit), perfect utilization of all interfacial area, and the full voltage appearing across every interface simultaneously. This last assumption is physically impossible in a percolating conductor network: when the conductive phase (carbon) forms a connected network, the applied voltage distributes unevenly across interfaces depending on local resistance, so most interfaces experience only a fraction of the total applied voltage. Realistic interfacial energy storage in carbon/metal oxide composites would be at least an order of magnitude below this upper bound, yielding approximately 1–10 Wh/kg — consistent with the performance of conventional electric double-layer capacitors.

Conclusion: Pure electrostatic energy storage — whether in bulk fields or at nanostructured interfaces — cannot account for energy densities of 200–400 Wh/kg at cell voltages of 1–4 V. **Any device in this voltage and energy density range must store the majority of its energy through a chemical mechanism, regardless of what it is called.**

3. Constraints from Published Third-Party Performance Data

Published test reports from an independent national research laboratory on a representative device in this class (a 3-cell bipolar pouch cell, nominal 26 Ah / 94 Wh, voltage range 2.7–4.3 V) provide the following constraints on the energy storage mechanism:

(a) Rate-dependent capacity. At 1C charge rate, discharge capacity was 26.1–26.5 Ah. At 5C, 26.0 Ah. At 11C, 25.6–25.9 Ah. In the fast-charge tests, a fixed charge of 26.0 Ah was delivered in each case; yet the device returned progressively less on discharge at higher charge rates. This indicates a slow storage mechanism that does not fully engage at high charge rates — some fraction of the delivered charge is not durably retained when charging time is insufficient.

(b) Cross-cycle balancing. A 1C reference cycle performed after 11C fast-charge tests delivered 26.52 Ah on discharge, while only 26.07 Ah had been charged on that cycle. The device returned more energy than was delivered in a single cycle, indicating that charge stored incompletely during prior fast charging had persisted in an intermediate state and was recovered during the subsequent slow cycling.

(c) Battery-like charge retention. The device retained 97.7% of stored capacity after 10 days of idle time. Voltage dropped 128 mV total, with most of the drop (116 mV) occurring in the first 10 hours and minimal additional drop over the remaining 230 hours. This two-phase retention profile is inconsistent with simple capacitor self-discharge (which would show continuous linear voltage decay) and suggests a combination of fast-relaxing and slow-relaxing components.

(d) Enhanced performance at elevated temperature. At 80°C, the device delivered 110% of its room-temperature capacity. At 100°C, 107%. This is consistent with a thermally-activated chemical process (faster kinetics allowing more complete reaction in the same charge time) and inconsistent with a purely electrostatic mechanism (where capacitance typically decreases at elevated temperature due to reduced dielectric constant).

(e) Zero electrochemical degradation. After loss of mechanical compression and 50 cycles at 5C, the device showed capacity loss due to mechanical delamination but no chemical degradation. The discharge/charge ratio returned to 1.0 and stabilized. The remaining capacity was perfectly stable. This indicates an extremely reversible storage mechanism with no parasitic side reactions.

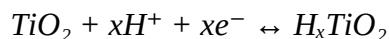
(f) Mechanical compression dependence. Capacity scaled with mechanical compression. Loss of compression reduced capacity to approximately 47% of the original value, where it stabilized. This indicates that the storage mechanism requires intimate physical contact between cell components but operates identically at every interface that maintains contact.

4. The Proton Intercalation Hypothesis

4.1 Rationale

Given that: (1) the energy must be stored chemically (Section 2); (2) devices in this class are reported to contain amorphous metal oxide and carbon processed from aqueous media; (3) if aqueous processing is used, bound water is inevitably present at oxide/carbon interfaces and within the amorphous oxide structure; and (4) published test data show no evidence of conventional metal-ion battery chemistry (no voltage plateaus, no SEI formation, no cycle-dependent degradation) — the most physically plausible mechanism is proton intercalation into the amorphous metal oxide, driven by the electric field across the device.

Proton intercalation into amorphous metal oxides, particularly amorphous TiO_2 , is well documented in the electrochromics and energy storage literature. The reaction is:



where x can reach 0.5–1.0 in amorphous structures. The reaction is highly reversible, involves minimal structural change in the disordered amorphous network (unlike crystalline intercalation compounds), and produces no phase transformations, no gas evolution, and no parasitic byproducts. The proton source is the bound water inherent to the amorphous oxide and to the oxide/carbon interface.

4.2 Quantitative Feasibility

The molecular weight of TiO_2 is 79.87 g/mol. At an intercalation depth of $x = 0.5$, the specific proton capacity is:

$$Q = 0.5 \times F / M = 0.5 \times 96,485 / 79.87 = 604 \text{ C/g} = 168 \text{ mAh/g}$$

At $x = 1.0$, the capacity is 335 mAh/g. Published values for proton intercalation into nanostructured amorphous TiO_2 range from 150 to 500 mAh/g depending on the morphology, surface area, and degree of hydration.

For a 3-cell bipolar stack delivering 26 Ah per cell (cells in series carry identical current), each cell requires 26 Ah of proton capacity in its active material. At 300 mAh/g, this requires approximately 87 g of amorphous TiO_2 per cell. For a device employing both electrodes and the separator as active proton-intercalating material (a continuous nanostructured composite with a proton concentration gradient across its thickness), the total active oxide mass per cell must be approximately 87 g.

The voltage per cell (~ 1.2 V, inferred from the 3.6 V nominal across 3 cells) must arise from the proton chemical potential difference between the protonated and deprotonated states of the oxide. Published values for the proton intercalation potential of amorphous TiO_2 relative to a standard hydrogen electrode range from 0.5 to 2.0 V depending on the material and the degree of protonation. A symmetric rocking-chair configuration, where one electrode loads protons while the other unloads them, would produce a cell voltage equal to the difference in proton chemical potential between the two loading states. A voltage of 1.2 V is within the published range.

The energy per cell is $E = Q \times V = 26 \text{ Ah} \times 1.2 \text{ V} = 31.2 \text{ Wh}$. For three cells in series: 93.6 Wh. This matches the nominal device specification of 94 Wh to within measurement uncertainty.

The energy density depends on the total cell mass. If the 3-cell stack mass is 235 g (consistent with the manufacturer's 400 Wh/kg claim), each cell weighs approximately 78 g, of which ~ 87 g would need to be active TiO_2 . This is not achievable — the active material alone would exceed the total cell mass. The 400 Wh/kg claim therefore requires either: (a) a lighter oxide with higher specific capacity; (b) a cell mass higher than implied by the headline energy density; or (c) a proton intercalation capacity at the high end of published values (~ 500 mAh/g), reducing the required oxide mass to ~ 52 g per cell, which is physically achievable in a 78 g cell with minimal inactive components.

The proton intercalation hypothesis is quantitatively feasible but requires that the active oxide achieve specific capacities at or near the highest values reported in the literature, and that inactive mass (current collectors, packaging, binder) be minimized through the screen-printed all-nanoparticle construction. Even at 500 mAh/g, the required ~ 52 g of oxide per cell in a 78 g cell would constitute approximately 67% of the total cell mass, leaving only ~ 26 g for carbon, binder, current collectors, separator, and packaging. This is demanding but may be achievable in a construction where all components are thin, screen-printed layers with no excess material.

4.3 Consistency with Observed Behavior

Rate-dependent capacity: Proton intercalation into amorphous oxide is a diffusion-limited process. At high charge rates, protons intercalate into the most accessible near-surface sites but do not penetrate to deeper bulk sites. Less total capacity is stored. At low rates, deeper sites are accessed and full capacity is achieved. This matches the observed decrease from 26.5 Ah at 1C to 25.7 Ah at 11C.

Cross-cycle balancing: Protons intercalated into near-surface sites during fast charging can slowly diffuse to deeper sites during subsequent rest or slow-rate cycling. This redistributed charge becomes available on subsequent discharge, explaining the 26.52 Ah reference cycle that exceeded the charge delivered on that cycle.

Charge retention: Intercalated protons occupy sites with binding energies significantly above thermal energy ($kT \approx 0.026$ eV at room temperature). Sites with estimated binding energies of 0.3–0.5 eV (reasonable for proton coordination at oxide defect sites in amorphous structures) would have deintercalation time constants of minutes to hours — accounting for the initial voltage drop in the first 10 hours. Deeper, more tightly bound sites would have deintercalation time constants of months to years, accounting for the flat retention over the remaining 230 hours. A distribution of site binding energies, which is expected in any amorphous material due to the inherent disorder in local atomic environments, would naturally produce the observed two-phase retention profile.

Temperature enhancement: Proton diffusion in amorphous oxide follows Arrhenius kinetics. Higher temperature increases diffusion rate, allowing more complete intercalation into deep sites within the same charge time. The 110% capacity at 80°C indicates that at room temperature, the charge rate used (1C) was insufficient to access all available sites — additional thermal activation revealed hidden capacity.

Zero degradation: Proton intercalation into amorphous TiO_2 produces negligible structural change because the disordered network accommodates the small proton without lattice strain. Unlike lithium intercalation into crystalline oxides, where repeated expansion and contraction degrades the crystal structure, proton insertion into an amorphous host is intrinsically non-damaging. This is consistent with the observed zero chemical degradation over 50 cycles at 5C.

Compression dependence: Proton intercalation requires intimate electronic contact between the carbon current-carrying network and the oxide active material for electron transfer, and intimate contact between the hydrated oxide and the proton source (bound water) for proton supply. Loss of mechanical compression breaks these contact interfaces, reducing the fraction of active material that can participate, without damaging the material at interfaces that maintain contact.

5. The Role of Bound Water

Amorphous metal oxides produced by aqueous processing inevitably contain bound water in multiple forms: surface hydroxyl groups (M–OH), structural water within the disordered lattice, and capillary-condensed water in nanoscale pores and interstices. This water is not a contaminant

but a functional component of the proposed mechanism, serving as the proton reservoir from which the intercalation reaction draws its charge carriers.

The Kelvin equation predicts that water condenses spontaneously from ambient humidity into nanoscale gaps between hydrophilic surfaces at dimensions below approximately 2 nm. In a nanostructured composite of carbon and amorphous oxide particles, such gaps are ubiquitous. The capillary-condensed water is thermodynamically stable — it cannot be removed without either heating above the oxide crystallization temperature (350–450°C for amorphous TiO_2) or reducing humidity to near zero. This explains why devices processed from aqueous media and equilibrated with ambient conditions would naturally contain the functional water layer.

The bound water also provides the protonic transport pathway from the reservoir to the intercalation sites. Proton transport through hydrogen-bonded water networks (Grotthuss mechanism) is rapid over nanometer distances and provides the kinetic pathway for fast charging. The combination of a thermodynamically stable proton reservoir (bound water), a rapid transport pathway (Grotthuss hopping over nanometer distances), and a reversible storage destination (amorphous oxide bulk sites) constitutes a self-contained proton storage system at every carbon/water/oxide interface in the nanocomposite.

A critical question is whether the bound water is electrochemically stable at the operating voltages involved. The tested device operates at up to 4.3 V across a 3-cell stack, implying approximately 1.43 V per cell. Bulk water electrolyzes at 1.23 V. The per-cell voltage therefore exceeds the thermodynamic electrolysis threshold by approximately 0.2 V. However, the water in this system is not bulk water: it is chemisorbed, structurally incorporated, and capillary-confined. The electrochemical stability of nanoconfined water at hydrophilic oxide surfaces is not well characterized and may differ significantly from the bulk value. Additionally, if the proton intercalation reaction is kinetically favored over the oxygen evolution reaction at the relevant surfaces, the system may be metastably protected even above the thermodynamic electrolysis potential. This question requires experimental investigation and represents the most significant uncertainty in the proposed mechanism.

6. The Capacitor Architecture as Driving Mechanism

Although the energy in the proposed mechanism is stored chemically, the capacitor architecture plays an essential role: the electric field generated by charge separation across the device drives the proton intercalation reaction. Without the field, there is no driving force for protons to leave their

equilibrium positions in the water network and intercalate into the oxide. The field provides the electrochemical overpotential that makes the reaction proceed.

This creates a coupled system. The capacitor field drives proton intercalation. The intercalated protons change the local electronic structure of the oxide (proton insertion creates donor states in the semiconductor), which modifies the local field distribution, which affects the driving force for further intercalation. Depending on the sign and magnitude of this feedback, the system may exhibit self-reinforcing behavior during charging — the storage mechanism becomes more efficient as it proceeds.

Observable signatures of this coupling would include: (a) a charge curve whose shape evolves during charging, reflecting the changing electrode properties; (b) an apparent capacitance that increases with state of charge rather than remaining constant; and (c) a voltage contribution from the internal semiconductor potential that adds to the externally applied capacitor voltage, producing terminal voltage that exceeds what pure charge separation would generate.

The semiconductor properties of the separator may play a role distinct from the electrodes. If the separator is a dense semiconducting oxide film rather than a porous nanocomposite, it could accept protons at one surface and release them at the other surface through changes in its surface electronic states, without requiring bulk proton transport across its thickness. This would enable macroscopic charge coupling between electrodes through a semiconductor relay mechanism — proton in on one face, electronic equilibration through the band structure, proton out on the other face. The rate of this process would be limited by the surface reaction kinetics rather than by bulk diffusion, which could explain the device's high-rate capability.

7. Experimentally Testable Predictions

The proton intercalation hypothesis makes the following predictions, each of which is testable with standard analytical techniques:

(a) Thermogravimetric analysis (TGA) of the electrode and separator materials should show mass loss corresponding to water and hydroxyl groups in the range 100–450°C, with the amount of water correlating with device performance. Devices dried aggressively at high temperature should show reduced capacity.

(b) Fourier-transform infrared spectroscopy (FTIR) should show O–H stretching bands in the electrode material, with changes in band position and intensity between charged and discharged states indicating proton redistribution.

(c) X-ray photoelectron spectroscopy (XPS) should show changes in the Ti 2p or equivalent metal oxide peak between charged and discharged states, consistent with reduction of the oxide upon proton intercalation.

(d) Electrochemical quartz crystal microbalance (EQCM) measurements during charge and discharge should show mass changes consistent with proton (1 g/mol) insertion and extraction rather than heavier metal ion intercalation.

(e) Isotope substitution: Replacing H₂O with D₂O in the processing or equilibration environment should produce a kinetic isotope effect — reduced charge rate and reduced high-rate capacity due to the slower diffusion of deuterons compared to protons. This would be strong evidence for proton involvement in the rate-limiting step.

(f) Humidity dependence: Device performance should depend on the ambient humidity during fabrication or equilibration. Devices sealed in dry conditions should show reduced capacity compared to devices equilibrated with ambient humidity, if bound water is the proton source.

(g) Rate-dependent capacity mapping: Systematic measurement of discharge capacity as a function of charge rate from 0.1C to 20C should reveal a characteristic capacity–rate curve whose shape reflects the proton diffusion kinetics into the oxide bulk. This curve can be fitted to standard diffusion models to extract the proton diffusion coefficient in the amorphous oxide.

8. Cation-Pi Interaction as a Candidate Energy Storage Contribution

The thermodynamic energy budget for proton intercalation into amorphous metal oxide, as analysed in Section 4.2, is tight at the energy densities reported for devices in this class. The chemical enthalpy of proton intercalation (30–100 kJ/mol), even with nanoscale enhancement and electric enthalpy contributions from concentrated local fields, approaches but does not comfortably exceed the approximately 116 kJ/mol per mole of protons required to account for the observed energy output. This section identifies an additional energy contribution that has not, to the author’s knowledge, been previously considered in the context of metal oxide/carbon energy storage: the cation-pi interaction between protons and the aromatic pi electron system of reduced graphene oxide.

8.1 The Cation-Pi Interaction

The cation-pi interaction is a non-covalent attraction between a positively charged ion and the face of an aromatic ring system. It arises from the electrostatic attraction between the cation and the quadrupole moment of the aromatic pi electron cloud, supplemented by polarization and charge-

transfer contributions. In biochemistry, cation- π interactions are recognised as one of the strongest non-covalent forces, governing ion channel selectivity, neurotransmitter binding, and protein folding. Published binding energies for cation- π interactions range from 20 to 80 kJ/mol depending on the cation, the aromatic system, and the environment, with protons (H^+) at the high end of this range due to their small size and high charge density.

8.2 Reduced Graphene Oxide as an Aromatic Substrate

Reduced graphene oxide is an extended aromatic system — a two-dimensional sheet of conjugated sp^2 carbon with a delocalised π electron cloud extending across the basal plane. Each hexagonal ring constitutes a potential cation- π binding site. Despite the presence of residual oxygen functional groups that locally disrupt the conjugation, rGO retains large aromatic domains (typically 2–10 nm across) separated by defect regions. The total aromatic surface area available for cation- π interactions in a nanostructured rGO electrode can reach hundreds of square metres per gram.

Cation- π interactions on graphene surfaces have been observed and reported in the surface science literature. Anomalously strong binding of cations to graphene has been noted in multiple studies. However, these studies have generally treated water as a solvent or background medium rather than as a functional component that defines the geometry of the interaction.

8.3 Bound Water as Geometric Spacer

The optimal distance for a cation- π interaction between a proton and a benzene ring in the gas phase is approximately 0.2–0.3 nm from the ring plane. A water monolayer is approximately 0.3 nm thick. This coincidence raises the possibility that bound water in the galleries between rGO sheets and amorphous metal oxide nanoparticles could position protons at or near the optimal distance for cation- π interaction with the rGO π system.

This proposal must be treated with caution. The optimal gas-phase distance may not apply in a condensed, hydrated environment where dielectric screening from the surrounding water would reduce the interaction energy. However, it is worth noting that if the dielectric constant of nanoconfined water is as low as 2–10 (as reported for sub-nanometer confinement [18]), the dielectric screening would be minimal, and the cation- π interaction energy in the confined environment could approach a substantial fraction of the gas-phase value. The actual geometry in a nanostructured rGO/metal oxide/water composite is complex and heterogeneous, not an idealised planar system. And the proton is not a bare ion — in the hydrated environment it exists as H_3O^+ or

within the hydrogen bond network, which modifies its effective charge distribution and its distance from the aromatic surface.

8.4 Potential Contribution to Energy Budget

If cation- π interactions contribute even 20–40 kJ/mol to the proton binding energy at rGO surfaces, this would close the thermodynamic deficit identified in Section 4.2 between the known proton intercalation enthalpy of amorphous TiO_2 and the total Gibbs free energy required to account for the observed device performance. Published density functional theory calculations on graphene models report gas-phase cation- π binding energies of 130–226 kJ/mol for alkali metal cations (Li^+ , Na^+ , K^+), with larger aromatic systems binding more tightly than smaller ones. Even with substantial aqueous screening reducing these values by 50–80%, the residual interaction energy of 30–100 kJ/mol in the hydrated environment would be more than sufficient. Furthermore, recent molecular dynamics simulations with first-principles accuracy have demonstrated that protons (as hydronium ions) preferentially accumulate at the graphene-water interface, driven by enthalpic forces that maintain the hydrogen bonding network while enabling energetically favorable interactions with the graphene π system. The cation- π contribution would be additive with the oxide intercalation enthalpy, the nanoscale enhancement, and the electric enthalpy, potentially explaining why devices using rGO as the carbonaceous substrate outperform those using activated carbon or other non-aromatic carbon forms.

This hypothesis is testable. Devices constructed with rGO (aromatic π system intact) should show higher energy density than otherwise identical devices constructed with activated carbon (disordered, largely non-aromatic). If the cation- π interaction is a significant contributor, nitrogen doping of the rGO — which disrupts the π conjugation — should reduce energy density despite potentially increasing electronic conductivity. Conversely, higher-quality rGO with larger aromatic domains should show higher energy density.

8.5 Connection to Published Research

Cation- π interactions on graphene and carbon nanotube surfaces have been studied computationally and experimentally in the context of water purification, ion transport, and molecular recognition. Multiple research groups have been active in carbon nanomaterials research, including graphene interactions with water and ions. The connection between these studied phenomena and energy storage performance in metal oxide/carbon composite devices has not, to the author's knowledge, been explicitly made in the published literature. The insight that bound water at the oxide/carbon interface may serve as a geometric spacer that positions protons at

the optimal cation- π interaction distance with the rGO aromatic system is proposed here as an original contribution.

The author emphasises that this proposal is a hypothesis, not a demonstrated mechanism. The actual cation- π interaction energy in the hydrated, nanoconfined environment of an rGO/metal oxide composite requires determination by computational methods (density functional theory or molecular dynamics simulation) or by experimental measurement (e.g., comparison of devices using aromatic versus non-aromatic carbon substrates). The hypothesis is presented because it is physically plausible, would resolve the thermodynamic deficit in the energy budget, and suggests specific testable predictions that could advance understanding of the energy storage mechanism in this class of devices.

9. Scope and Limitations

This paper does not claim to identify the specific materials or construction of any particular commercial device. No device has been disassembled or analyzed by the author. The analysis is based entirely on published third-party electrical performance data and established physics.

The paper does claim, with quantitative certainty, that electrostatic field energy cannot account for the reported performance of devices in this class. This is a mathematical result, not an assumption or hypothesis.

The proton intercalation hypothesis is presented as the most physically plausible mechanism consistent with the available constraints, not as a proven explanation. Alternative mechanisms that are also chemically-based — such as reversible surface redox reactions, ion adsorption at functionalized interfaces, or other intercalation chemistries — are not excluded. The critical conclusion is that the mechanism must be chemical, not electrostatic, and that any adequate explanation must quantitatively account for 26 Ah of charge storage at 3.6 V in a device of the reported mass.

The role of bound water, the semiconductor properties of the separator, and the coupled field-chemistry feedback mechanism described in Sections 5 and 6 are hypotheses that require experimental validation. They are presented because they are consistent with the available data and because they suggest specific, testable predictions (Section 7) that could confirm or refute them.

10. Conclusions

The quantitative analysis presented in this paper leads to three conclusions of decreasing certainty:

First, with mathematical certainty: no device operating at 1–4 V can store 200–400 Wh/kg of energy electrostatically. The energy density of electric fields at these voltages is too low by many orders of magnitude, regardless of dielectric constant, electrode surface area, or nanostructure. Any device achieving these energy densities stores its energy chemically.

Second, with high plausibility: in a system containing amorphous metal oxide, carbon, and bound water from aqueous processing, the most likely chemical mechanism is proton intercalation into the amorphous oxide. This mechanism is well-documented in the literature, is quantitatively feasible at the required capacity if the oxide achieves specific capacities near the high end of published values, and is consistent with every published third-party observation: rate-dependent capacity, cross-cycle balancing, two-phase charge retention, temperature-enhanced performance, zero degradation, and compression dependence.

Third, as hypothesis: the capacitor architecture of these devices is not incidental but essential — the electric field drives the proton intercalation, and the intercalation modifies the semiconductor properties of the oxide, creating a coupled feedback mechanism that produces the anomalous combination of capacitor-like charging behavior and battery-like energy density. The separator may function as a semiconductor relay that couples the two electrodes through surface proton exchange without bulk proton transport.

Fourth, as speculative proposal: cation- π interactions between protons and the aromatic π electron system of reduced graphene oxide may contribute a significant additional energy component (20–40 kJ/mol per proton) to the total energy stored, with bound water at the oxide/carbon interface potentially acting as a geometric spacer that positions protons near the optimal interaction distance from the rGO aromatic surface. This contribution, which connects well-established cation- π binding physics from biochemistry with graphene/water interfacial science in a novel energy storage context, would resolve the thermodynamic deficit in the proton intercalation energy budget and predicts that devices using aromatic carbon substrates (rGO, graphene) should outperform otherwise identical devices using non-aromatic carbon substrates (activated carbon, carbon black). This prediction is directly testable and, if confirmed, would identify the aromatic character of the carbonaceous substrate as a previously unrecognised design parameter for energy storage devices in this class.

These conclusions are experimentally testable through the methods described in Section 7 and the comparative experiments proposed in Section 8. The author invites the scientific community to investigate, challenge, and refine the analysis presented here.

10.1 Statement on Public Availability

This paper is published to place the analysis, hypotheses, and theoretical framework it contains into the public domain. The author believes that the fundamental science of energy storage mechanisms should be freely available to all researchers, engineers, manufacturers, and nations. The transition to sustainable energy storage is a global imperative that transcends commercial competition. If the mechanisms described here prove correct, they imply that high-density energy storage can be achieved using only globally abundant, non-toxic, inexpensive materials — titanium, carbon, water, aluminum — processed with simple equipment in ambient air. No nation, corporation, or individual should have exclusive control over the scientific understanding of such a technology. The author expressly intends this publication to serve as prior art preventing the patenting of the fundamental mechanisms described herein, including field-driven proton storage in amorphous metal oxide, cation- π energy storage at graphene-water interfaces, capillary-condensed water as a functional component in energy storage electrodes, and the coupled field-chemistry feedback mechanism. Specific device implementations, material formulations, and manufacturing processes remain patentable; the science does not.

Appendix: References

Cation- π Interactions

- [1] Dougherty, D.A. “The Cation- π Interaction.” *Chemical Reviews*, 2024. (Comprehensive review of cation- π interactions in chemistry and biology, including graphene systems. Citing Mu et al., reports gas-phase DFT binding energies of 54, 40, and 31 kcal/mol for Li⁺, Na⁺, and K⁺ on a graphene model (C₈H₄24), with binding strength increasing for larger aromatic systems.)
- [2] Zhao, G. et al. “Cation- π Interactions in Graphene-Containing Systems for Water Treatment and Beyond.” *Advanced Materials*, vol. 32, 2020, 1905756. (Overview of cation- π interactions on graphene surfaces, including cross-linking effects, membrane stability, and adsorption enhancement.)
- [3] Chen, J. et al. “Hydrated cation- π interactions of π -electrons with hydrated Li⁺, Na⁺, and K⁺ cations.” *Physical Chemistry Chemical Physics*, 2021. (DFT study showing graphene can distort hydration shells for direct cation- π contact with K⁺, while Li⁺ interacts through water mediation.)
- [4] Shi, G. et al. “Non-covalent interactions of graphene surface: Mechanisms and applications.” *Chem (Cell Press)*, vol. 8, 2022. (Comprehensive review of ion- π interactions on graphene, including cation- π and anion- π interactions, with discussion of divalent cations binding more strongly than monovalent.)
- [5] Fang, H.-P. et al. “Highly Efficient Ion Rejection by Graphene Oxide Membranes Based on Cation- π Interactions.” *ACS Nano*, vol. 8, 2014, pp. 850–859. (Demonstrates that cation- π interactions control interlayer spacing in GO membranes, with hydrated Li⁺ adsorption energy of -26.3 kcal/mol between graphene sheets.)

Protons at Graphene-Water Interfaces

- [6] “Protons Accumulate at the Graphene–Water Interface.” *ACS Nano*, 2025. (Machine learning-based molecular dynamics simulations with first-principles accuracy demonstrating that hydronium ions preferentially

accumulate at the graphene-water interface, driven by enthalpic forces that maintain the hydrogen bonding network. Hydroxide ions show bimodal distribution. Confinement effects also examined.)

- [7] Otten, D.E., Shaffer, P.R., Geissler, P.L., Saykally, R.J. “Mechanism of ion adsorption to aqueous interfaces: Graphene/water vs. air/water.” *Proceedings of the National Academy of Sciences*, vol. 114, no. 51, 2017, pp. 13369–13374. (University of California, Berkeley. Demonstrates that direct ion/graphene interactions dominate the favorable enthalpy of ion adsorption at the graphene-water interface.)

Amorphous TiO₂ for Energy Storage

- [8] “Lithium Storage in Amorphous TiO₂ Nanoparticles.” *Journal of the Electrochemical Society*, vol. 157, 2010, pp. A1099–A1104. (Reports extraordinary initial discharge capacity of 810 mAh/g for amorphous TiO₂ nanoparticles, stabilizing at ~200 mAh/g. XAS reveals Ti⁴⁺ to Ti^{3.5+} reduction upon ion insertion.)
- [9] Wang, S. et al. “Interface-strain-confined synthesis of amorphous TiO₂ mesoporous nanosheets with stable pseudocapacitive lithium storage.” *Chemical Engineering Journal*, vol. 422, 2021, 130049. (Demonstrates high pseudocapacitive capability and long cycling stability of amorphous TiO₂ nanosheets, 103 mAh/g at 6 A/g after 1000 cycles. Demonstrates that interfacial strain can stabilize the amorphous phase against crystallization.)
- [10] Bella, F., Lamberti, A. et al. “Unveiling the controversial mechanism of reversible Na storage in TiO₂ nanotube arrays: Amorphous versus anatase TiO₂.” *Nano Research*, vol. 10, 2017, pp. 3892–3906. (Politecnico di Torino. Compares amorphous and crystalline TiO₂ for sodium storage, demonstrating intrinsically different electrochemical responses between the two phases.)
- [11] Ylhäinen, E.K., Nunes, M.R., Silvestre, A.J., Monteiro, O.C. “Synthesis of titanate nanostructures using amorphous precursor material and their adsorption/photocatalytic properties.” *Journal of Materials Science*, 2012. (Tampere University of Technology and University of Lisbon. Hydrothermal synthesis of titanate nanostructures from amorphous TiO₂ precursors, demonstrating aqueous-route preparation of nanostructured titanium oxide materials.)
- [12] Zhang, Y. et al. “Nanostructured TiO₂ Arrays for Energy Storage.” *Materials*, vol. 16, 2023, 3864. (Hainan University. Comprehensive review of TiO₂ nanoarray synthesis methods and energy storage applications in batteries and supercapacitors.)

Third-Party Device Performance Data

- [13] Independent national research laboratory. “Solid-State Energy Storage Device V1 Charge Performance Test.” Report CR-00092-26, February 2026. (Independent fast-charge testing at 5C and 11C rates. Nominal capacity 26 Ah, nominal energy 94 Wh. Publicly available test report.)
- [14] Independent national research laboratory. “Solid-State Energy Storage Device V1 High Temperature Performance Test.” Report CR-00124-26, March 2026. (110% of nominal capacity at 80°C, 107% at 100°C. Cell pouch lost vacuum after 100°C test; electrochemistry unaffected. Publicly available test report.)
- [15] Independent national research laboratory. “Solid-State Energy Storage Device V1 Self-Discharge Test.” Report CR-00125-26, March 2026. (97.7% charge retention after 10 days. Two-phase voltage decay: 116 mV drop in first 10 hours, minimal additional drop over remaining 230 hours. Publicly available test report.)
- [16] Independent national research laboratory. “Solid-State Energy Storage Device V1 Safety Demonstration Test.” Report CR-00178-26, March 2026. (50 cycles at 5C on vacuum-damaged cell. Capacity dropped from ~25 Ah to ~11 Ah then stabilized. Zero chemical degradation. Discharge/charge ratio returned to 1.0. Publicly available test report.)

Capillary Condensation and Nanoconfined Water

- [17] Thomson, W. (Lord Kelvin). “On the Equilibrium of Vapour at a Curved Surface of Liquid.” *Philosophical Magazine*, 1871. (Foundation of the Kelvin equation describing capillary condensation in nanopores.)
- [18] Fumagalli, L. et al. “Anomalously low dielectric constant of confined water.” *Science*, vol. 360, 2018, pp. 1339–1342. (Demonstrates that the dielectric constant of nanoconfined water drops to approximately 2 for water confined to layers less than ~ 1 nm, relevant to the discussion of confined water properties at oxide/carbon interfaces.)

Maxwell–Wagner–Sillars Polarization

- [19] Maxwell, J.C. *A Treatise on Electricity and Magnetism*, 1873. (Original description of interfacial polarization in heterogeneous dielectrics.)
- [20] Wagner, K.W. “Erklärung der dielektrischen Nachwirkungsvorgänge auf Grund Maxwellscher Vorstellungen.” *Archiv für Elektrotechnik*, vol. 2, 1914, pp. 371–387. (Extension of Maxwell’s interfacial polarization theory to layered dielectric systems.)
- [21] Sillars, R.W. “The properties of a dielectric containing semi-conducting particles of various shapes.” *Journal of the Institution of Electrical Engineers*, vol. 80, 1937, pp. 378–394. (Extension to particulate composites with arbitrary particle geometry.)

Industry and Commercial Context

- [22] Patent WO2025230455A1, “Flexible solid energy storage module.” Filed May 2, 2025, published November 6, 2025. (Screen-printed solid-state energy storage with nanoparticle electrodes and polymeric binder. Excludes lithium, cobalt, nickel, cadmium, and rare earth elements. No specific active materials or energy storage mechanism disclosed.)
- [23] Independent national research laboratory. Press release, February 20, 2026. (Confirms that the laboratory conducted measurements on a commercially developed solid-state energy storage cell as an independent testing service. Results published publicly by the device manufacturer.)

Note: This reference list is representative, not exhaustive. The author has relied on publicly available data, established physics, and published peer-reviewed literature. No proprietary or confidential information from any commercial entity has been used in the preparation of this paper.